JACS
JOURNAL OF THE AMERICAN CHEMICAL SOCIETY
pubs.acs.org/JACS
Article

Mechanism of Ultrafast Triplet Exciton Formation in Single Cocrystals of π-Stacked Electron Donors and Acceptors

Malik L. Williams, Itai Schlesinger, Robert M. Jacobberger, and Michael R. Wasielewski*

Cite This: J. Am. Chem. Soc. 2022, 144, 18607−18618
Read Online
ACCESS | Metrics & More | Article Recommendations | Supporting Information

ABSTRACT: Ultrafast triplet formation in donor−acceptor (D−A) systems typically occurs by spin−orbit charge-transfer intersystem crossing (SOCT-ISC), which requires a significant orbital angular momentum change and is thus usually observed when the adjacent π systems of D and A are orthogonal; however, the results presented here show that subnanosecond triplet formation occurs in a series of D−A cocrystals that form one-dimensional cofacial π stacks. Using ultrafast transient absorption microscopy, photoexcitation of D−A single cocrystals, where D is coronene (Cor) or pyrene (Pyr) and A is *N*,*N*-bis(3′-pentyl)-perylene-3,4:9,10-bis(dicarboximide) (C_5PDI) or naphthalene-1,4:5,8-tetracarboxydianhydride (NDA), results in formation of the charge transfer (CT) excitons $Cor^{\bullet+}$-$C_5PDI^{\bullet-}$, $Pyr^{\bullet+}$-$C_5PDI^{\bullet-}$, $Cor^{\bullet+}$-$NDA^{\bullet-}$, and $Pyr^{\bullet+}$-$NDA^{\bullet-}$ in <300 fs, while triplet exciton formation occurs in τ = 125, 106, 484, and 958 ps, respectively. TDDFT calculations show that the SOCT-ISC rates correlate with charge delocalization in the CT exciton state. In addition, time-resolved EPR spectroscopy shows that $Cor^{\bullet+}$-$C_5PDI^{\bullet-}$ and $Pyr^{\bullet+}$-$C_5PDI^{\bullet-}$ recombine to form localized ^{3}*C_5PDI excitons with zero-field splittings of $|D|$ = 1170 and 1250 MHz, respectively. In contrast, $Cor^{\bullet+}$-$NDA^{\bullet-}$ and $Pyr^{\bullet+}$-$NDA^{\bullet-}$ give triplet excitons in which $|D|$ is only 1240 and 690 MHz, respectively, compared to that of NDA (2091 MHz), which is the lowest energy localized triplet exciton, indicating that the Cor-NDA and Pyr-NDA triplet excitons have significant CT character. These results show that charge delocalization in CT excitons impacts both ultrafast triplet formation as well as the CT character of the resultant triplet states.

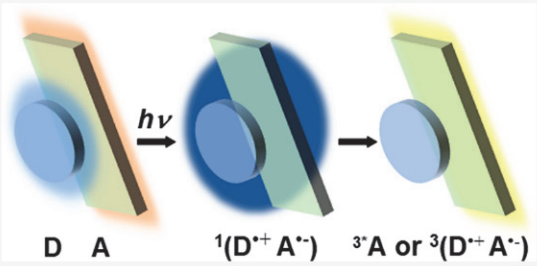

INTRODUCTION

Interest in organic donor−acceptor (D−A) cocrystals for potential electronic and photonic applications[1−3] is growing rapidly due to the ease of designing cocrystals having properties such as ferroelectricity,[4,5] ambipolar charge transport,[1,6−10] photonic waveguiding,[11−13] tunable emission,[1,14−17] and near-infrared absorption.[18] Early work on triplet excitons in D−A cocrystals focused largely on their diffusion through quasi-1D π-stacks, degree of charge transfer (CT) character, and decay kinetics.[19−28] Recent studies have dealt with CT intermediates in singlet fission,[29,30] triplet−triplet annihilation leading to photon upconversion,[31,32] and applications in photodynamic therapy.[33−35]

Surprisingly, no studies to date have examined the rate and mechanism of triplet formation in single D−A cocrystals. Spin−orbit-induced intersystem crossing (SO-ISC) is usually responsible for triplet formation in organic chromophores; however, singlet fission (SF), radical pair ISC (RP-ISC), and spin−orbit charge transfer ISC (SOCT-ISC) can also result in triplet formation.[35−38] SF is a spin-allowed, down-conversion process involving two chromophores that results in the formation of two triplet excitons following absorption of one photon and requires favorable energetics. It has been shown that low-lying interchromophore CT states promote SF through state mixing; however, if the CT state energies are below that of the lowest excited singlet state, they competitively inhibit SF.[39,40] In contrast, RP-ISC occurs following electron transfer within donor−acceptor (D−A) systems and requires weak spin−spin exchange and dipolar interactions in $D^{\bullet+}$−$A^{\bullet-}$.[41] Thus, both processes are unlikely in a π-stacked radical ion pair. SOCT-ISC is typically observed in D−A systems in which the D and A π systems are nearly orthogonal.[42−44] In that case, ultrafast ISC occurs because CT is accompanied by a large change in orbital angular momentum, which must be offset by a change in spin angular momentum to conserve total angular momentum.[45]

Given that planar D and A molecules usually crystallize into cofacially π-stacked one-dimensional ...DADA... columns, this geometry is believed to strongly disfavor SOCT-ISC because the π orbitals of D and A are parallel to one another. For example, we found recently that photoexcitation of a D−A cocrystal in which D = *peri*-xanthenoxanthene (PXX) and A = *N*,*N*-bis(3′-pentyl)-2,5,8,11-tetraphenyl-perylene-3,4:9,10-bis(dicarboximide) (Ph_4PDI), where D and A are cofacially π-

Received: August 12, 2022
Published: September 30, 2022

stacked, does not produce a measurable triplet yield.[46] In contrast, several groups have recently found that SOCT-ISC can occur in cofacial D−A systems; yet a mechanism that accounts for SOCT-ISC in this D−A geometry has not be studied.[38,47,48]

To address this apparent contradiction, we have studied triplet exciton formation dynamics in a series of donor−acceptor cocrystals using coronene (Cor) and pyrene (Pyr) donors each paired with either a *N*,*N*-bis(3′-pentyl)perylene-(3,4:9,10)-bis(dicarboximide) (C_5PDI) or a naphthalene-1,4:5,8-tetracarboxydianhydride (NDA) acceptor (Scheme 1)

Scheme 1. Structures of the Electron Donors and Acceptors Used in This Study

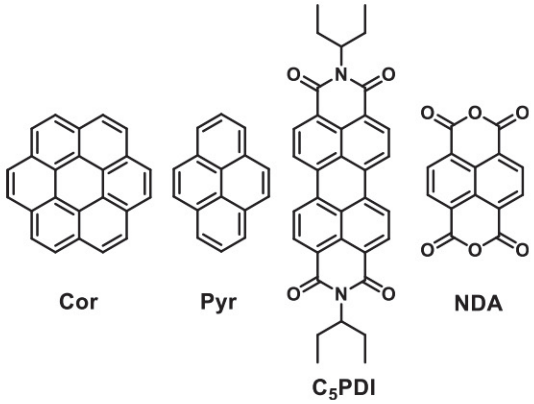

using transient absorption microscopy (TAM)[46,49] and time-resolved electron paramagnetic resonance (TREPR) spectroscopy. We find that charge delocalization in the CT exciton state is most likely responsible for the angular momentum change that results in ultrafast triplet formation in these cocrystals. In addition, we find that the resulting triplet excitons produced in the Cor-C_5PDI and Pyr-C_5PDI cocrystals are localized on a single C_5PDI, whereas the triplet excitons of Cor-NDA and Pyr-NDA retain significant CT character. This provides an opportunity to design new molecular materials with tailored triplet exciton production for optoelectronic applications.

EXPERIMENTAL METHODS

Single Crystal Structure Determination. Cor, Pyr, and NDA, and perylene-3,4:9,10-tetracarboxydianhydride (PDA) were obtained from Sigma-Aldrich, while C_5PDI was prepared from PDA as described earlier.[50] Cor and C_5PDI were cocrystallized from chloroform and methanol, while Cor and NDA as well as Pyr and NDA were cocrystallized by slow cooling from a dimethyl sulfoxide solution that had been heated to reflux.

The crystal structure of the Pyr-C_5PDI was reported earlier.[51] A suitable single crystal of Cor-C_5PDI (0.6 × 0.08 × 0.03 mm^3), Cor-NDA (0.047 × 0.185 × 0.450 mm^3), or Pyr-NDA (0.061 × 0.085 × 0.465 mm^3) was mounted on a MiTeGen loop with paratone oil on an XtaLAB Synergy diffractometer equipped with a microfocus rotating-anode Rigaku Cu X-ray source, and a Hybrid Pixel Array Detector (HyPix) detector. The temperature of the crystal was controlled at 100 K with an Oxford Cryostat. Following data collection, data reduction was performed with CrysAlisPro software using an empirical absorption correction. The structure was solved with the ShelXT[52] structure solution program using the Intrinsic Phasing solution method and by using Olex2 as the graphical interface. The model was refined with ShelXL[52] using least-squares minimization. Highly disordered solvent molecules were removed using the solvent mask program in OLEX2.[53] The structures of the Cor-C_5PDI, Cor-NDA, and Pyr-NDA cocrystals were deposited in the Cambridge Crystallographic Data Center (CCDC 2082407, 2190090, and 2190085, respectively). Additional crystallographic data are provided in the Supporting Information, Tables S1−S3, and Figures S1−S5.

Powder X-ray Diffraction Measurements. PXRD data were collected at room temperature on a STOE-STADI-P powder diffractometer equipped with an asymmetric curved Germanium monochromator (CuKα1 radiation, λ = 1.54056 Å) and one-dimensional silicon strip detector (MYTHEN2 1K from DECTRIS). The line focused Cu X-ray tube was operated at 40 kV and 40 mA. Powder was packed in a 3 mm metallic mask and sandwiched between two polyimide layers of tape. Intensity data from 5 to 40 degrees two theta were collected over a period of 30 min. The instrument was calibrated against a NIST Silicon standard (640d) prior the measurement.

Steady-State Absorption and Emission Spectroscopy. Steady-state absorption spectra were collected on the cocrystals using a Xenon arc lamp (Oriel Instruments, model 66902). The beam was spatially filtered through a pinhole and polarized using a Glan−Thompson polarizer. A motorized (ELL14K, Thorlabs) achromatic half-wave plate (SAQWP05M-700, Thorlabs) was used to rotate the linear polarization. The beam was then sent into the back port of an upright microscope (Eclipse Ti−U, Nikon). In the microscope the beam was directed through an internal mirror to a 15× reflective objective lens (LMM15X, Thorlabs) to focus on the sample. The transmitted part was collected using a second objective lens and then sent to a home-built spectrometer (Richardson Gratings, 52A15BK-224C) and focused onto a fast line-scan camera (OctoPlus, Teledyne e2v), sampling at 100 000 lines/s. For absorption measurements, a reference spectrum (on bare glass) and a transmission spectrum (through a single cocrystal) were collected for each polarization in the range 0−360° in 10° steps. A dark spectrum, with no light on the sample, was subtracted from all reference and transmission spectra.

For emission measurements, the output of an optical parametric amplifier (see next section) was set to the wavelengths indicated in Figure 2 and ∼1 μW using a neutral density filter. The beam was focused on the sample and recollected employing the same setup used for steady-state absorption measurements. To resolve the weak emission, the integration time on the line-scan camera was set to the maximum of 655 ms.

Femtosecond Transient Absorption Microscopy (fsTAM). The 1040 nm output from a commercial Yb:KGW, 4 W, 100 kHz repetition rate, 300 fs, amplified laser system (Spirit-One, Spectra-Physics) was divided into two beams. One beam was sent to an optical parametric amplifier (OPA) (Spirit-OPA-8, Light Conversion) to generate the pump beam wavelengths indicated in Figure 4. The pump was sent to a quarter-wave plate, which converted it to a circularly polarized beam, and then into an electro-optic amplitude modulator (EO-AM-NR-C4, Thorlabs), which was phase-synchronized to the laser output and a polarizer to amplitude-modulate the beam at 50 kHz. The laser pulses passing through the EOM suffer severe time stretching of up to a few ps; thus, a lab-built two-prism compressor was used to recompress them to ∼200 fs as measured using a lab-built autocorrelator. The other 1040 nm beam was sent to a double-pass linear delay line (Newport, IMS600LM), and then focused into an 8 mm thick undoped YAG crystal for white light continuum generation. The beam was then recollimated and the fundamental was removed using a 1000 nm short-pass filter. The pump and probe beams were coaxially combined using a 50:50 beamsplitter and sent into the microscope system and spectrometer described above. The polarizations of the pump and the probe beams were varied independently using two achromatic half-wave plates. The pump and probe power on the sample were each set to 2 μW using two neutral density filters. The pump and probe focused spot size (4 standard deviations of a Gaussian, or 95% of the beam intensity) on the sample were 2.9 μm, giving pump and probe fluence of 0.6 mJ/cm^2 and 0.3 mJ/cm^2, respectively. To further mitigate systematic baseline shifts during the measurement, the TA spectrum at each

https://doi.org/10.1021/jacs.2c08584
J. Am. Chem. Soc. 2022, 144, 18607−18618

delay point was individually referenced to a fixed negative delay point (−10 ps).

Nanosecond Transient Absorption Microscopy (nsTAM). A nanosecond-pulsed 405 nm laser (NPL41B, Thorlabs) was used as a pump. The laser output was combined with the same white light continuum beam used in the fsTAM apparatus, and both beams were sent to the microscope through the same optical path as described above. The pump−probe delay was electronically modified using a delay generator (DG645, Stanford Research). The pump was electronically triggered at 50 kHz using lab-built electronics.

Data Analysis and Global Fitting. The TA data on each cocrystal were chirp-corrected in a lab-written Python software by fitting time-zero to a third order polynomial. All data were globally fit using a previously described MATLAB fitting program.[54]

Time-Resolved Electron Paramagnetic Resonance (TREPR) Spectroscopy. Time-resolved electron paramagnetic resonance (TREPR) studies of Cor-C_5PDI, Pyr-C_5PDI, Cor-NDA, and Pyr-NDA were performed at 293, 40, 50, and 85 K, respectively, and at X-band microwave frequency (9.59 GHz) using a Bruker Elexsys E580 EPR spectrometer equipped with a split-ring resonator (ER4118X-MS3). A powder of each cocrystal was sealed in a quartz EPR tube (inner and outer diameters of 2.0 and 2.4 mm, respectively) under a vacuum of 10^{-3} Torr. Powdered cocrystals were employed because the single cocrystals were too small to obtain TREPR spectra. The samples were photoexcited at the wavelengths indicated in Figure 6 with 7 ns, 2 mJ laser pulses using an optical parametric oscillator (Basi-scan, Spectra-Physics) pumped with the 355 nm output of a frequency-tripled, 10 Hz Nd:YAG laser (Quanta-Ray Lab 170, Spectra-Physics). Following photoexcitation, kinetic traces of the transient magnetization were acquired as a function of the magnetic field in both the real and imaginary detection channels (i.e., quadrature detection) under continuous microwave irradiation of 5.0 mW. The data were processed by first subtracting the signal prior to the laser pulse for each kinetic trace (at a given magnetic field) and then subtracting the signal at off-resonance magnetic fields for each spectrum (at a given time). The spectra are fit using the *pepper* function in EasySpin 5.2.35.[55]

TDDFT Calculations. Calculations were performed on Cor-C_5PDI, Pyr-C_5PDI, Cor-NDA, and Pyr-NDA D−A pairs using time-dependent density functional theory (TDDFT) in QChem 5.1.[56] The geometry and relative orientation of the donors and acceptors in the cocrystals were taken directly from the X-ray crystallographic data without further optimization. Single point energy calculations were performed using the ωB97X-D3 functional, 6-31G* basis set, and random phase approximation for configuration interaction single transitions. Orbital contributions and spin densities were all calculated in Multiwfn 3.8.[57]

RESULTS AND DISCUSSION

Cocrystal Structures. Cor and C_5PDI were recently found to cocrystallize in quasi-1D π-stacks in either 1:1 or 2:1 molecular ratios depending on the growth method, stoichiometric ratios, and specific PDI derivative used.[7,58] Cocrystallizing equimolar amounts of Cor or Pyr with C_5PDI and Cor or Pyr with NDA in all cases results in dark red, rod-like crystals (Figures S1−S3 and ref S1), whose structures were determined using single-crystal X-ray diffraction (Figures 1 and S4). All four D−A cocrystals form quasi-1D DADA... π-stacks that are aligned along the cocrystal long axes with average interplanar distances between D and A of 3.36−3.65 Å (Figure 1). Additional X-ray diffraction data on all cocrystals are presented in Figures S1−S5 and Tables S1−S3. PXRD data obtained on all four crystals agrees very well with the PXRD pattern simulated using the X-ray diffraction crystal structure data (Figure S6).

Steady-State Absorption and Emission Data. The polarization-dependent, steady-state electronic absorption spectra of each cocrystal are given in Figure 2, while the corresponding polar plots are shown in Figure S7. The Cor-C_5PDI cocrystal shows several prominent maxima at 510, 553, and 597 nm along with a weaker, broad absorption at about 650 nm (Figure 2a). Similar spectral features in Cor-bis(*N*,*N*-cyclohexyl)PDI cocrystals have been observed using unpolarized light.[58] These intense bands are strongly red-shifted relative to the reddest absorptions of Cor (430 nm)[59] and C_5PDI (520 nm). Given that Cor and C_5PDI are π-stacked at near van der Waals distances, these shifts most likely result from a strong CT interaction between the Cor electron donor and the C_5PDI electron acceptor with the band at 650 nm being the lowest energy CT transition.[60] The photoluminescence (PL) spectrum exhibits a maximum at 710 nm (Figure 2a). The energy average of the 650 nm CT absorption and 710 nm PL band yields a CT state energy of 1.83 eV. Data for the Pyr-C_5PDI cocrystal were reported earlier,[51] and in that case, the Pyr-C_5PDI CT band comparable to that of Cor-C_5PDI is not observed because its transition dipole moment (TDM) is nearly perpendicular to the crystallographic *a*-axis, which is parallel to the glass substrate surface, and is thus nearly orthogonal to all orientations of the polarized light.[46] In addition, the orientation of the C_5PDI TDM[61] is ∼40° relative to the crystallographic *a*-axis, so that the C_5PDI absorption of the cocrystal exhibits a modest dependence of the polarized light orientation. The sharp absorption band at 410 nm may result from the red-shifted pyrene absorption in the solid state. The unpolarized PL spectrum of the Pyr-C_5PDI single cocrystal shows a band maximum at 710 nm, which is assigned to the CT emission in the cocrystal and indicates that the CT state energy is also about 1.8 eV (Figure 2b).

The Cor-NDA cocrystal displays broad absorption bands with maxima at 545 and 590 nm (Figure 2c), while the Pyr-NDA cocrystal has similar bands at 557 and 592 nm (Figure 2d).[61] These bands are significantly red-shifted from the absorption bands of Cor (430 nm),[59] Pyr (335, 370 nm),[62] and NDA (380 nm)[63] and are thus attributed to a strong CT interaction between the Cor or Pyr donors and the NDA acceptor. The unpolarized PL spectra of the Cor-NDA and Pyr-NDA cocrystals have single broad bands with maxima at 712 and 683 nm, respectively, which are assigned to CT emission (Figures 2c and 2d). The energy average of the absorption and photoluminescence bands yields CT state energies of 1.92 and 1.93 eV for the Cor-NDA and Pyr-NDA cocrystals, respectively.

Charge Transfer Energetics. The one-electron oxidation potentials of Cor and Pyr are both 1.2 V vs SCE,[64] while the one-electron reduction potentials of C_5PDI and NDA are both −0.5 V vs SCE.[63] The difference between these two potentials

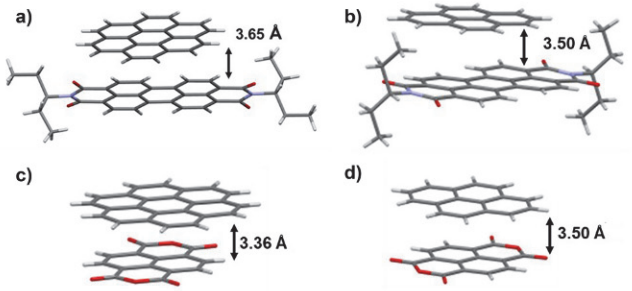

Figure 1. X-ray crystal structures of (a) Cor-C_5PDI, (b) Pyr-C_5PDI, (c) Cor-NDA, and (d) Pyr-NDA cocrystals.

https://doi.org/10.1021/jacs.2c08584
J. Am. Chem. Soc. 2022, 144, 18607−18618

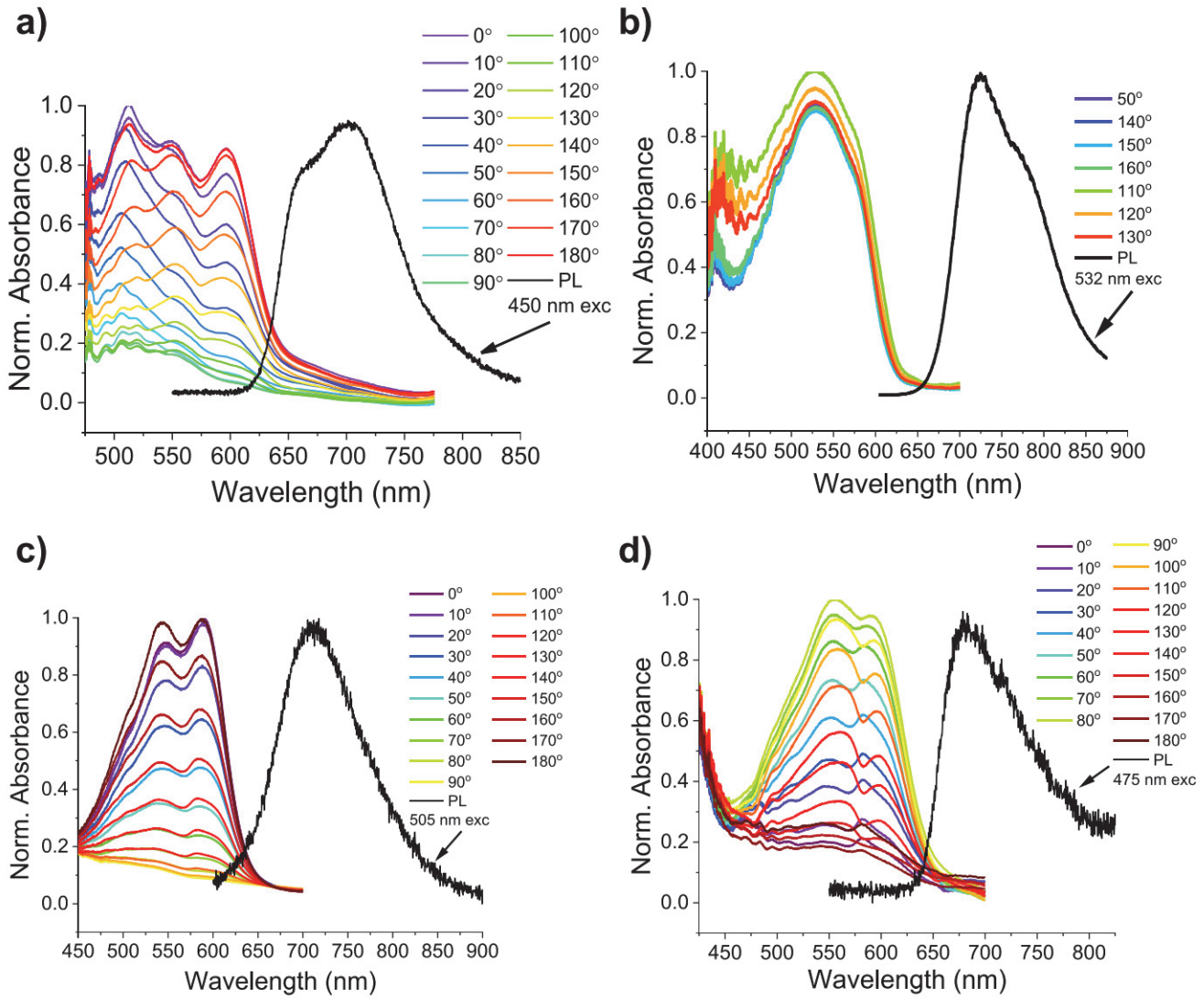

Figure 2. Polarization-resolved steady-state absorption and unpolarized PL spectra of (a) Cor-C_5PDI, (b) Pyr-C_5PDI, (c) Cor-NDA, and (d) Pyr-NDA cocrystals. The angles given refer to the polarization direction of the linearly polarized light relative to the long axis of the cocrystal.

is approximately the CT state energy in a polar solvent, which for all four D−A pairs is 1.7 eV. The optical spectra of all four cocrystals show that their CT state energies are about 0.1−0.2 eV higher than that estimated from the redox potentials. Weller has shown that for a $D^{\bullet+}$−$A^{\bullet-}$ pair at a fixed distance the CT state energy decreases relative to that predicted by the redox potentials as a result of the Coulombic attraction of the two ions.[65] However, this decrease is more than compensated by the increase in CT state energy due to the low polarity of the cocrystal environment relative to the polar solvents in which the redox potentials are measured.[65] The cocrystals described here have the advantage that the strong D−A CT interactions result in absorption and emission bands from which the CT energies can be determined directly rather than relying on the assumptions intrinsic to the Weller treatment. The energetics are summarized in Figure 3.

Transient Absorption Microscopy. FsTAM and nsTAM data were obtained on single cocrystals of Cor-C_5PDI, Pyr-C_5PDI, Cor-NDA, and Pyr-NDA by exciting each cocrystal at a wavelength (λ_{exc}) where the cocrystal absorption is nearly independent of pump polarization (Figure 2). For each cocrystal, the short wavelength limit of the data is determined

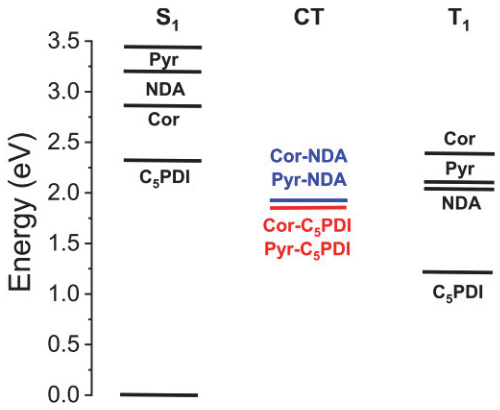

Figure 3. Measured energy levels of the Cor-C_5PDI, Pyr-C_5PDI, Cor-NDA, and Pyr-NDA cocrystal CT states as well as the lowest excited singlet (S_1) and triplet (T_1) state energies of their constituent donors and acceptors. The blue lines and labels denote the nearly degenerate energies of the Cor-NDA and Pyr-NDA CT states, while the red lines and labels denote the nearly degenerate energies of the Cor-C_5PDI and Pyr-C_5PDI CT states.

https://doi.org/10.1021/jacs.2c08584
J. Am. Chem. Soc. 2022, 144, 18607−18618

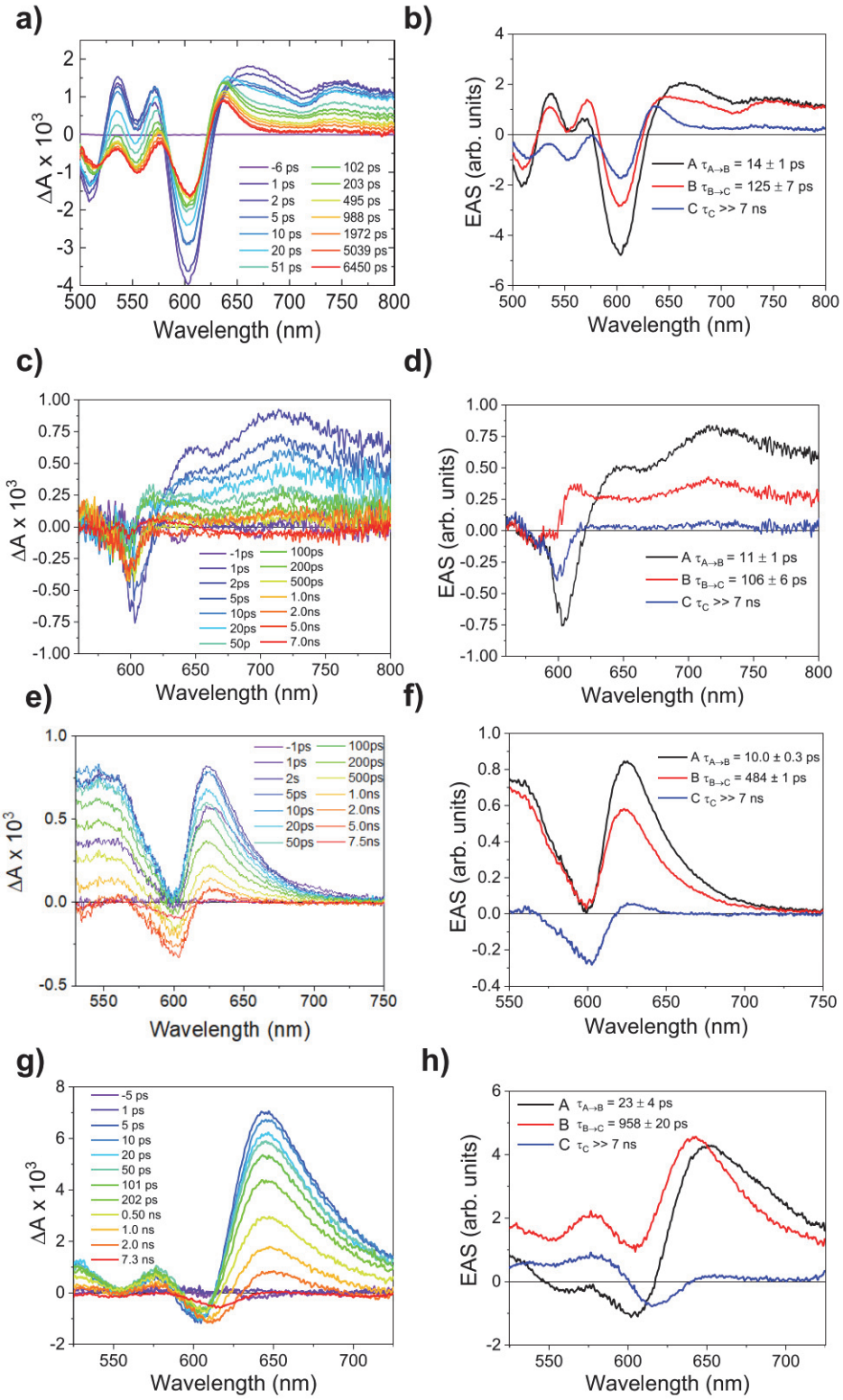

Figure 4. FsTAM data for single cocrystals. (a,c,e,g) FsTAM spectra vs pump−probe delay time for Cor-C_5PDI (λ_{exc} = 450 nm), Pyr-C_5PDI (λ_{exc} = 450 nm), Cor-NDA (λ_{exc} = 475 nm), and Pyr-NDA (λ_{exc} = 475 nm), respectively, where the probe beam is polarized parallel to the crystal long axis. (b,d,f,h) Normalized evolution-associated spectra for Cor-C_5PDI, Pyr-C_5PDI, Cor-NDA, and Pyr-NDA, respectively, using an A → B → C state model. Plots of kinetics at selected wavelengths and normalized populations as a function of time are given in Figure S8.

largely by the intensity of the white light probe pulse as well as the optical density of the cocrystal. Photoexcitation of the Cor-C_5PDI cocrystal at 450 nm results in ground-state bleaches (GSB) at 510, 555, and 604 nm, as well as excited state absorption (ESA) from 660 to 800 nm characteristic of $C_5PDI^{\bullet-}$ (Figure 4a).[66] The $Cor^{\bullet+}$ absorption occurs at 465 nm in solution and is mostly likely blue of the 500 nm probe limit of this experiment.[67] These absorption changes appear in

https://doi.org/10.1021/jacs.2c08584
J. Am. Chem. Soc. 2022, 144, 18607−18618

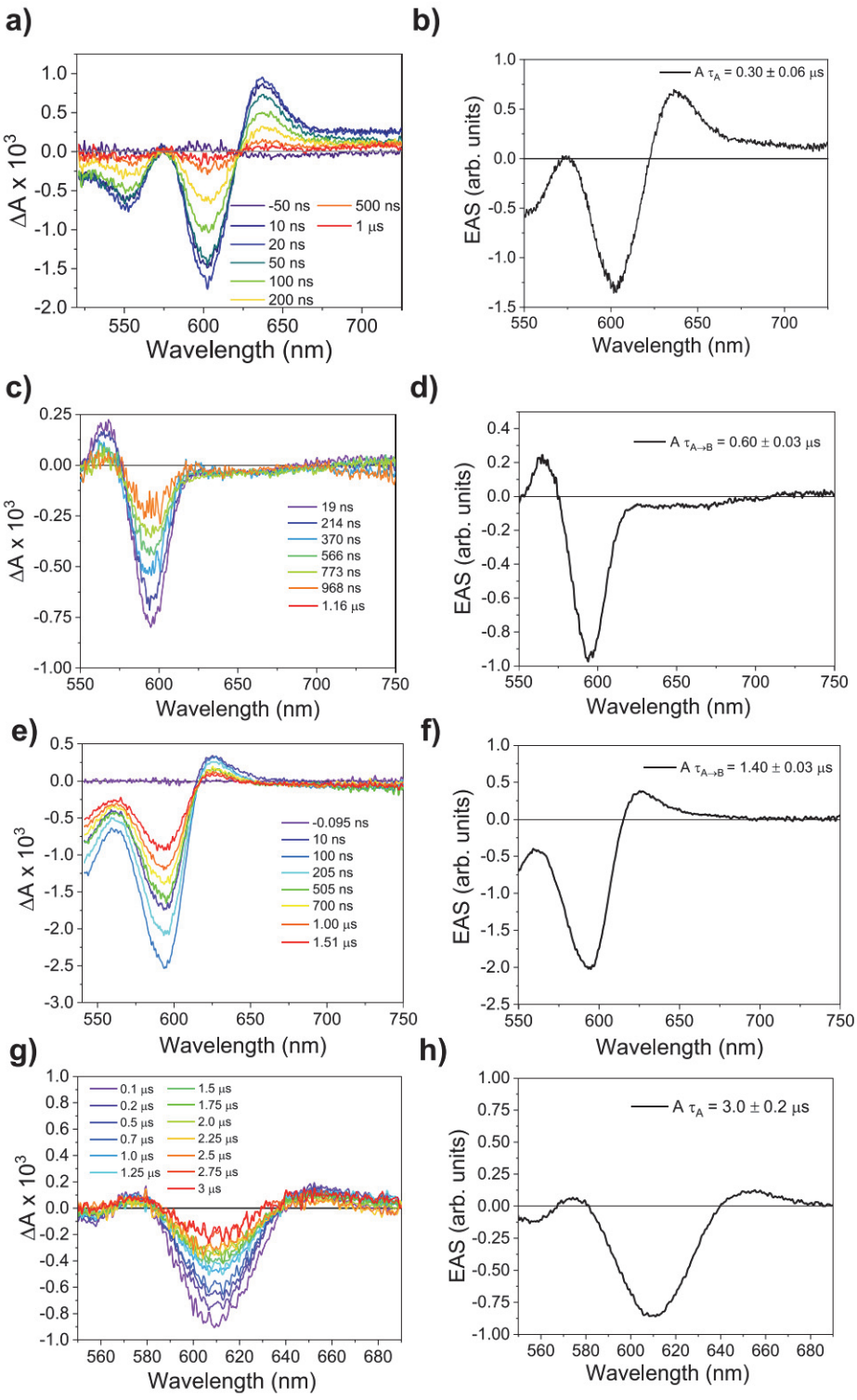

Figure 5. NsTAM data for single cocrystals excited with a 405 nm, 6 ns pulse. (a,c,e,g) NsTAM spectra vs pump−probe delay time for Cor-C_5PDI, Pyr-C_5PDI, Cor-NDA, and Pyr-NDA, respectively, where the probe beam is polarized parallel to the crystal long axis. (b,d,f,h) Normalized evolution-associated spectra for Cor-C_5PDI, Pyr-C_5PDI, Cor-NDA, and Pyr-NDA, respectively, using an A → ground state model. Plots of kinetics at selected wavelengths and normalized populations as a function of time are given in Figure S9.

<300 fs and decay to leave the ground state bleaches overlapping and canceling part of a broad ESA extending from 500 to 670 nm, which lives beyond the 7 ns pump−probe delay time. Since the 500−670 nm band is spectrally similar to the ESA of ^{3}*PDI seen in PDI films[68] and is long-lived, we assign it to the formation of ^{3}*C_5PDI in the cocrystal. This assignment is confirmed by TREPR measurements described below. Global fitting of the data using an A → B → C model yields the evolution-associated spectra (EAS) shown in Figure 4b. Species A is assigned to a hot CT exciton Cor$^{\bullet+}$-C_5PDI$^{\bullet-}$

https://doi.org/10.1021/jacs.2c08584
J. Am. Chem. Soc. 2022, 144, 18607−18618

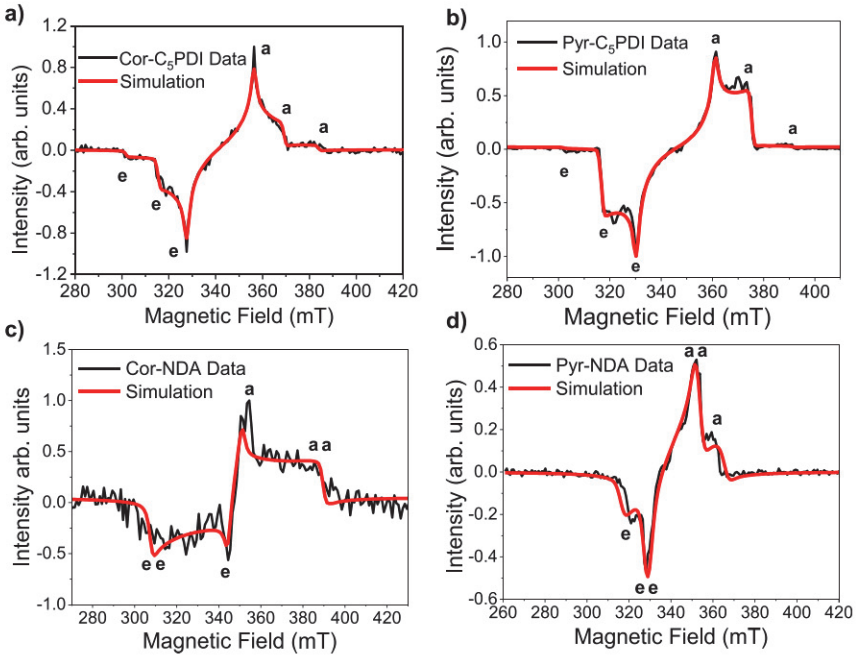

Figure 6. TREPR spectra and simulated spectra of powdered (a) Cor-C_5PDI, (b) Pyr-C_5PDI, (c) Cor-NDA, and (d) Pyr-NDA cocrystals at 293, 40, 50, and 85 K, respectively, obtained 100 ns after a 7 ns laser pulse at 675, 600, 635, and 600 nm, respectively.

that relaxes in $\tau_{A\rightarrow B}$ = 14 ± 1 ps to species B, the relaxed CT exciton. Rapid intersystem crossing accompanies charge recombination of the relaxed CT exciton in $\tau_{B\rightarrow C}$ = 125 ± 7 ps to produce ^{3}*C_5PDI in about a 37% yield based on a comparison of the initial GSB to that of the triplet exciton at long times (Figure S11). A comparable data set for a Cor-C_5PDI cocrystal using 630 excitation is given in Figure S11, which yields similar results. NsTAM data show that ^{3}*C_5PDI decays to ground state in τ = 0.30 ± 0.06 μs (Figures 5a and 5b).

The fsTAM data obtained on the Pyr-C_5PDI cocrystal following photoexcitation at 450 nm results in the formation of the Pyr$^{\bullet+}$-C_5PDI$^{\bullet-}$ hot CT exciton in τ < 300 fs as indicated once again by the GSB at 604 nm and the broad ESA at 700 nm due to C_5PDI$^{\bullet-}$ formation (Figure 4c). Pyr$^{\bullet+}$ absorbs at 453 nm with weak bands in the near-infrared,[69] so it is unlikely that the observed absorption changes have significant contributions from this radical cation in the 525−800 nm wavelength range accessible in this experiment. The observed transient spectra, which have significantly higher signal-to-noise ratios than those we reported earlier,[51] decay to leave the GSB that overlaps and cancels part of a broad ESA extending from 525 to 600 nm. These absorption changes survive ≫7 ns and are also assigned to ^{3}*C_5PDI on the basis of the TREPR spectra described below. The apparent blue-shift of the relatively weak ^{3}*C_5PDI transient spectrum in Pyr-C_5PDI relative to that of Cor-C_5PDI results once again from the fact that the TDM of ^{3}*C_5PDI is about 40° relative to the glass substrate surface.[51] The EAS are shown in Figure 4d. Species A is assigned to a hot Pyr$^{\bullet+}$-C_5PDI$^{\bullet-}$ CT exciton that relaxes in $\tau_{A\rightarrow B}$ = 11 ± 1 ps to the relaxed CT exciton, species B. Rapid intersystem crossing accompanies charge recombination of the relaxed CT exciton in $\tau_{B\rightarrow C}$ = 106 ± 6 ps to produce ^{3}*C_5PDI in 43% yield (Figure S11). NsTAM data show that ^{3}*C_5PDI decays to ground state in τ = 0.60 ± 0.03 μs (Figures 5c and 5d).

The fsTAM spectra of a single Cor-NDA cocrystal show a strong GSB of the cocrystal absorption at 600 nm, which cancels out part of the ESA that appears at 525−750 nm (Figure 4e). The absorption that extends out to 750 nm is consistent with the absorption of NDA$^{\bullet-}$,[63] while, once again, the Cor$^{\bullet+}$ most likely absorbs at wavelengths bluer than our 525 nm probe limit in this experiment.[67] These absorption changes appear in <300 fs, which implies that the hot Cor$^{\bullet+}$-NDA$^{\bullet-}$ CT exciton is formed immediately upon photoexcitation. The EAS are shown in Figure 4f, where species A is the hot exciton that decays to the relaxed CT exciton, species B, in $\tau_{A\rightarrow B}$ = 10.0 ± 0.3 ps. These bands decay in $\tau_{B\rightarrow C}$ = 484 ± 1 ps to a long-lived GSB at 600 nm accompanied by weak ESA with maxima at 560 and 627 nm. It is likely that the GSB is canceling out the relatively weak absorption of ^{3}*NDA that occurs in this spectral region. This long-lived species is assigned to ^{3}*NDA based on its triplet TREPR spectra shown below and is produced in a 41% yield (Figure S11). The nsTAM spectra show that ^{3}*NDA decays to ground state in τ = 1.40 ± 0.03 μs (Figures 5e and 5f).

FsTAM spectra of a single Pyr-NDA cocrystal once again show the appearance in <300 fs of ground state bleach features at 560 and 605 nm accompanied by formation of a strong ESA with an apparent maximum at 652 nm that is partially canceled out by the GSB (Figure 4g). The EAS are shown in Figure 4h, where species A is the hot Pyr$^{\bullet+}$-NDA$^{\bullet-}$ CT exciton that decays to the cooled Pyr$^{\bullet+}$-NDA$^{\bullet-}$ CT exciton, species B, in $\tau_{A\rightarrow B}$ = 23 ± 4 ps. The relaxed CT state then decays in $\tau_{B\rightarrow C}$ = 958 ± 20 ps to form a long-lived species characterized by an ESA from 525 to 700 nm superimposed on the ground state bleach at 617 nm, which is consistent with the formation of ^{3}*NDA. As is the case for the Cor-NDA cocrystal, the long-lived species is assigned to ^{3}*NDA based on the triplet TREPR spectra obtained for this species shown below and is produced in a 46% yield (Figure S11). The nsTAM spectra show that

https://doi.org/10.1021/jacs.2c08584
J. Am. Chem. Soc. 2022, 144, 18607−18618

^{3}*NDA decays to ground state in $\tau = 3.0 \pm 0.2$ μs (Figures 5g and 5h).

Triplet State EPR Spectroscopy. Time-resolved electron paramagnetic resonance (TREPR) spectroscopy was used to characterize the long-lived triplet excitons formed in the D−A cocrystals. Since the single cocrystals were too small to obtain high quality TREPR spectra, a powdered sample of each cocrystal was examined. Following photoexcitation of the powdered cocrystals, a triplet TREPR spectrum is observed at 100 ns (Figure 6), in which the six-line spectrum of the triplet exciton is spin polarized with an (e,e,e,a,a,a) spectral powder pattern from low to high magnetic field, where (a) and (e) designate enhanced absorptive and emissive signals, respectively. The triplet TREPR spectra of the cocrystals are shown at temperatures for which the signal-to-noise is optimal; however, the observed zero-field splittings, $|D|$ and $|E|$, do not depend significantly on temperature.

The simulated spectrum for the Cor-C_5PDI cocrystal (Figure 6a, red line) closely matches the experimental spectrum when the zero-field splittings of the triplet are $|D|$ = 1170 MHz and $|E|$ = 120 MHz, which are typical for ^{3}*PDI derivatives ($|D|$ = 1274 MHz and $|E|$ = 130 MHz).[70] Similarly, the simulation of the TREPR spectrum of the triplet state resulting from charge recombination of Pyr$^{\bullet+}$-C_5PDI $^{\bullet-}$ gives $|D|$ = 1250 MHz and $|E|$ = 130 MHz, which again are similar to those of ^{3}*PDI (Figure 6b). Assuming $D > 0$, the spin polarization pattern indicates that SOCT-ISC selectively populates the T_x and T_y spin sublevels of the triplet manifold.[71] In contrast, simulation of the experimental TREPR spectrum resulting from charge recombination of Cor$^{\bullet+}$-NDA$^{\bullet-}$ in Figure 6c reveals that $|D|$ = 1240 MHz and $|E|$ = 350 MHz, in which $|D|$ is substantially reduced relative to that of both ^{3}*Cor ($|D|$ = 2910 MHz and $|E|$ = 0 MHz)[72] and ^{3}*NDA ($|D|$ = 2091 MHz and $|E|$ = 51 MHz).[73] Similarly, the TREPR spectrum of the triplet state resulting from charge recombination of Pyr$^{\bullet+}$-NDA$^{\bullet-}$ gives $|D|$ = 690 MHz and $|E|$ = 9 MHz, in which $|D|$ again is substantially smaller than that of ^{3}*Pyr ($|D|$ = 1852 MHz and $|E|$ = 202 MHz)[74] and ^{3}*NDA (Figure 6d). The (e,e,e,a,a,a) polarization pattern is characteristic of SOCT-ISC and thus rules out singlet fission[75] and radical pair intersystem crossing[71] as the mechanism for the fast triplet formation because they result in a characteristic (a,e,e,a,a,e) polarization pattern.

A decrease in $|D|$ relative to the value expected for an isolated chromophore triplet state is usually attributed to CT interactions with a neighboring molecule in which a triplet charge transfer state mixes with the neutral triplet state localized on the chromophore. This increases the average distance between the two electrons comprising the triplet exciton resulting in a smaller electron−electron dipolar interaction, and hence, a smaller $|D|$. For Cor-C_5PDI and Pyr-C_5PDI, $|D|$ decreases by about 8% and 2%, respectively, while for Cor-NDA and Pyr-NDA these decreases are far more substantial, 41% and 63%, respectively. These data show that the triplet exciton in the latter two cases has a high degree of CT character.

Mechanism of Triplet Exciton Formation. The rapid formation of triplet excitons in these cocrystals is somewhat surprising given that ordinary SO-ISC in organic chromophores occurs typically with rates on the order of 10^6−10^9 s^{-1}.[76] For example, it is especially slow in PDI derivatives, leading to triplet yields typically <1%.[58] As noted above, another potential explanation for fast triplet generation is SOCT-ISC,[35,38,48,77] in which photoexcitation of a D−A pair results in ultrafast ^{1}(D$^{\bullet+}$−A$^{\bullet-}$) formation followed by charge recombination directly to ^{3}*D−A or D−^{3}*A, if there is a change in the orbital angular momentum resulting from the electron transfer. However, the question remains: how does the needed angular momentum change occur in a π-stacked, cofacial D−A cocrystal? We propose a mechanism for ultrafast SOCT-ISC in these cocrystals that considers the differing orbital interactions between the donor and the acceptor that result in charge delocalization within the CT state influenced by the D−A π-stacking geometry.

Despite the fact that the D−A pairs are all nearly cofacial, the crystal structures of the cocrystals given in Figures 1 and S4 show that the degree of slip-stacking and rotation of the donor plane relative to that of the acceptor about the π-stacking axis is different in each cocrystal, and in no case are the two π-systems symmetrically placed on top of one another. TDDFT calculations were used to determine the electron distributions in the HOMO and LUMO of each cocrystal D−A pair using a Mulliken population analysis (Figure 7). These calculations

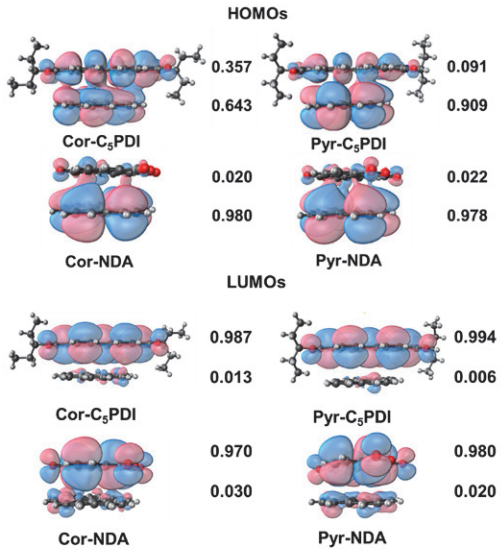

Figure 7. Calculated HOMOs and LUMOs for the indicated donor−acceptor pairs with the relative Mulliken populations on the donor and acceptor.

show that the HOMOs of the four D−A pairs have electron density that is shared to varying degrees between the donors and the acceptors, whereas the corresponding LUMOs are localized largely on the acceptors. The HOMOs of Cor-C_5PDI and Pyr-C_5PDI have 36% and 9%, respectively, of their electron density on the C_5PDI acceptor, while those of Cor-NDA and Pyr-NDA have 2% of their electron density residing on the NDA acceptor. The hole is delocalized along the π-stacking axis, which we will label the z-axis, while the electron remains localized. When charge recombination occurs, both charges are now confined to motion in the x−y plane of the acceptor π system, resulting in an angular momentum change that requires a spin angular moment change to conserve total angular momentum.

The smaller charge delocalization calculated for Cor-NDA and Pyr-NDA suggests that the rates of triplet exciton formation should be slower for these two cocrystals relative to Cor-C_5PDI and Pyr-C_5PDI, which is borne out by

https://doi.org/10.1021/jacs.2c08584
J. Am. Chem. Soc. 2022, 144, 18607−18618

experiment. However, in making these comparisons one must also consider the free energy changes. The free energy change upon charge recombination of $Cor^{\bullet+}$-$C_5PDI^{\bullet-}$ and $Pyr^{\bullet+}$-$C_5PDI^{\bullet-}$ to the corresponding triplet excitons is $\Delta G = -0.6$ eV. Since the internal reorganization energy for charge recombination in both cases is about 0.5 eV,[78−80] and there is no solvent contribution, the rate of recombination to the triplet exciton should be near the maximum of the Marcus rate vs free profile,[81,82] so that the rate of triplet exciton formation is not limited by ΔG. In contrast, given that the angular momentum changes for charge recombination of $Cor^{\bullet+}$-$NDA^{\bullet-}$ and $Pyr^{\bullet+}$-$NDA^{\bullet-}$ are smaller and $\Delta G \cong 0$ eV for these processes, the charge recombination rates to the triplet exciton for these systems are slower and retain significant CT character as shown by the significant reduction in their $|D|$ values obtained from TREPR spectroscopy.

The latter conclusion is also supported by TDDFT calculations of the triplet state spin densities on the donor and acceptor for the triplet excitons generated in the cocrystals (Figure 8). The calculations predict that for Cor-C_5PDI and

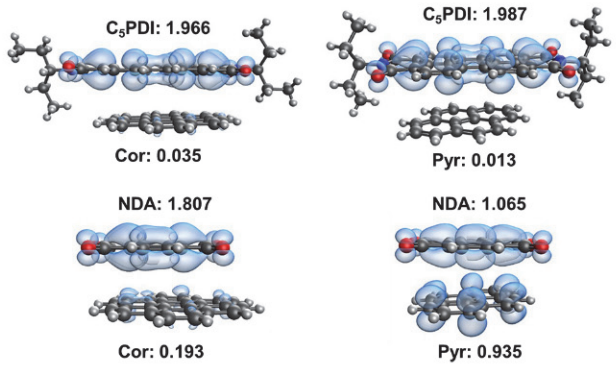

Figure 8. Calculated spin densities on D and A in ^{3}*(D−A) using TDDFT.

Pyr-C_5PDI, the triplet is almost entirely localized on C_5PDI, which agrees very well with the experimental $|D|$ values for the triplets formed upon charge recombination of $Cor^{\bullet+}$-$C_5PDI^{\bullet-}$ and $Pyr^{\bullet+}$-$C_5PDI^{\bullet-}$. In contrast, the TDDFT calculations predict 19% CT character for Cor-^{3}*NDA triplet exciton, while the triplet exciton produced in the Pyr-NDA cocrystals is almost a pure CT triplet exciton $^3(Pyr^{\bullet+}$-$NDA^{\bullet-})$. Once again, these predictions are in concert with the significant decreases in the $|D|$ values observed by TREPR for the triplet states of the NDA-containing pairs.

CONCLUSIONS

Ultrafast transient absorption microscopy shows that photoexcitation of Cor-C_5PDI, Pyr-C_5PDI, Cor-NDA, and Pyr-NDA single cocrystals produces CT excitons in <300 fs followed by subnanosecond charge recombination leading to SOCT-ISC in each cocrystal. SOCT-ISC is usually observed when the π systems of D and A are orthogonal; however, rapid SOCT-ISC in these cocrystals is a consequence of initial charge delocalization along the π-stacking direction followed by an orbital angular momentum change upon charge recombination that elicits a rapid spin angular momentum change to conserve total angular momentum. Charge recombination of the $Cor^{\bullet+}$-$C_5PDI^{\bullet-}$ and $Pyr^{\bullet+}$-$C_5PDI^{\bullet+}$ CT excitons produces ^{3}*C_5PDI in which the triplet exciton is localized on C_5PDI. In contrast, charge recombination of $Cor^{\bullet+}$-$NDA^{\bullet-}$ produces Cor-^{3}*NDA, which has 19% CT character as determined using TDDFT calculations, while subnanosecond ISC produces the long-lived CT triplet exciton $^3(Pyr^{\bullet+}$-$NDA^{\bullet-})$ with nearly complete charge separation (94%). TREPR spectra of the resulting triplet states in the cocrystals all display a spin polarization pattern characteristic of triplet formation by spin−orbit charge-transfer intersystem crossing (SOCT-ISC) and zero-field splitting $|D|$ values in agreement with the TDDFT predictions regarding CT contributions to the triplet excitons. We conclude that ultrafast triplet generation in 1D, π-stacked, D−A single cocrystals depends critically on the orbital interactions of D and A, as determined by their crystal structures, so that D−A single cocrystals can be designed to promote triplet exciton formation as needed for particular electronic or photonic applications.

ASSOCIATED CONTENT

Supporting Information

The Supporting Information is available free of charge at https://pubs.acs.org/doi/10.1021/jacs.2c08584.

Additional X-ray crystallography data, crystal images, transient optical data, and computational results (PDF)

Accession Codes

CCDC 2082407, 2190085, and 2190090 contain the supplementary crystallographic data for this paper. These data can be obtained free of charge via www.ccdc.cam.ac.uk/data_request/cif, or by emailing data_request@ccdc.cam.ac.uk, or by contacting The Cambridge Crystallographic Data Centre, 12 Union Road, Cambridge CB2 1EZ, UK; fax: +44 1223 336033.

AUTHOR INFORMATION

Corresponding Author

Michael R. Wasielewski − *Department of Chemistry and Institute for Sustainability and Energy at Northwestern, Northwestern University, Evanston, Illinois 60208-3113, United States;* orcid.org/0000-0003-2920-5440; Email: m-wasielewski@northwestern.edu

Authors

Malik L. Williams − *Department of Chemistry and Institute for Sustainability and Energy at Northwestern, Northwestern University, Evanston, Illinois 60208-3113, United States;* orcid.org/0000-0003-2835-4946

Itai Schlesinger − *Department of Chemistry and Institute for Sustainability and Energy at Northwestern, Northwestern University, Evanston, Illinois 60208-3113, United States;* orcid.org/0000-0003-4039-7885

Robert M. Jacobberger − *Department of Chemistry and Institute for Sustainability and Energy at Northwestern, Northwestern University, Evanston, Illinois 60208-3113, United States*

Complete contact information is available at: https://pubs.acs.org/10.1021/jacs.2c08584

Notes

The authors declare no competing financial interest.

ACKNOWLEDGMENTS

This work was supported by the National Science Foundation under Award No. DMR-2003739. We thank Mr. Jonathan R. Palmer for assistance with the TDDFT calculations. The

authors thank Profs. Vladimiro Mujica (Arizona State University), Roel Tempelaar (Northwestern University), and Gemma C. Solomon (University of Copenhagen) for stimulating discussions of this problem.

REFERENCES

(1) Han, X.; Wang, L.; Xi, G. Attractive organic cocrystal materials in optics. *Heterocycles* **2021**, *102*, 825−849.
(2) Huang, Y. J.; Wang, Z. R.; Chen, Z.; Zhang, Q. C. Organic cocrystals: Beyond electrical conductivities and field-effect transistors (FETS). *Angew. Chem., Int. Ed.* **2019**, *58*, 9696−9711.
(3) Wang, Y.; Zhu, W. G.; Dong, H. L.; Zhang, X. T.; Li, R. J.; Hu, W. P. Organic cocrystals: New strategy for molecular collaborative innovation. *Top. Curr. Chem.* **2016**, *374*, 1−83.
(4) Bolla, G.; Dong, H. L.; Zhen, Y. G.; Wang, Z. H.; Hu, W. P. Organic cocrystals: The development of ferroelectric properties. *Sci. China-Mater.* **2016**, *59*, 523−530.
(5) Wang, Z.; Zhang, Q. Organic donor-acceptor cocrystals for multiferroic applications. *Asian J. Org. Chem.* **2020**, *9*, 1252−1261.
(6) Park, S. K.; Varghese, S.; Kim, J. H.; Yoon, S. J.; Kwon, O. K.; An, B. K.; Gierschner, J.; Park, S. Y. Tailor-made highly luminescent and ambipolar transporting organic mixed stacked charge-transfer crystals: An isometric donor-acceptor approach. *J. Am. Chem. Soc.* **2013**, *135*, 4757−4764.
(7) Sato, R.; Yoo, D.; Mori, T. 1:2 charge-transfer complexes of perylene and coronene with perylene diimide, and the ambipolar transistors. *CrystEngComm* **2019**, *21*, 3218−3222.
(8) Su, Y. J.; Li, Y.; Liu, J. G.; Xing, R. B.; Han, Y. C. Donor-acceptor cocrystal based on hexakis (alkoxy)triphenylene and perylenediimide derivatives with an ambipolar transporting property. *Nanoscale* **2015**, *7*, 1944−1955.
(9) Zhang, J.; Tan, J. H.; Ma, Z. Y.; Xu, W.; Zhao, G. Y.; Geng, H.; Di, C. A.; Hu, W. P.; Shuai, Z. G.; Singh, K.; Zhu, D. B. Fullerene/sulfur-bridged annulene cocrystals: Two-dimensional segregated heterojunctions with ambipolar transport properties and photoresponsivity. *J. Am. Chem. Soc.* **2013**, *135*, 558−561.
(10) Zhu, L. Y.; Yi, Y. P.; Li, Y.; Kim, E. G.; Coropceanu, V.; Bredas, J. L. Prediction of remarkable ambipolar charge-transport characteristics in organic mixed-stack charge-transfer crystals. *J. Am. Chem. Soc.* **2012**, *134*, 2340−2347.
(11) Zhu, W.; Zhang, X.; Hu, W. Molecular cocrystal odyssey to unconventional electronics and photonics. *Science Bulletin* **2021**, *66*, 512−520.
(12) Zhu, W. G.; Zheng, R. H.; Fu, X. L.; Fu, H. B.; Shi, Q.; Zhen, Y. G.; Dong, H. L.; Hu, W. P. Revealing the charge-transfer interactions in self-assembled organic cocrystals: Two-dimensional photonic applications. *Angew. Chem., Int. Ed.* **2015**, *54*, 6785−6789.
(13) Zhu, W. G.; Zhu, L. Y.; Zou, Y.; Wu, Y. S.; Zhen, Y. G.; Dong, H. L.; Fu, H. B.; Wei, Z. X.; Shi, Q.; Hu, W. P. Deepening insights of charge transfer and photophysics in a novel donor-acceptor cocrystal for waveguide couplers and photonic logic computation. *Adv. Mater.* **2016**, *28*, 7563−7563.
(14) Sun, Y. Q.; Lei, Y. L.; Sun, X. H.; Lee, S. T.; Liao, L. S. Charge-transfer emission of mixed organic cocrystal microtubes over the whole composition range. *Chem. Mater.* **2015**, *27*, 1157−1163.
(15) Usman, R.; Khan, A.; Wang, M.; Luo, Y.; Sun, W.; Sun, H.; Du, C.; He, N. Investigation of charge-transfer interaction in mixed stack donor-acceptor cocrystals toward tunable solid-state emission characteristics. *Cryst. Growth Des.* **2018**, *18*, 6001−6008.
(16) Wykes, M.; Park, S. K.; Bhattacharyya, S.; Varghese, S.; Kwon, J. E.; Whang, D. R.; Cho, I.; Wannemacher, R.; Luer, L.; Park, S. Y.; Gierschner, J. Excited state features and dynamics in a distyrylbenzene-based mixed stack donor-acceptor cocrystal with luminescent charge transfer characteristics. *J. Phys. Chem. Lett.* **2015**, *6*, 3682−3687.
(17) Yan, D. P.; Delori, A.; Lloyd, G. O.; Friscic, T.; Day, G. M.; Jones, W.; Lu, J.; Wei, M.; Evans, D. G.; Duan, X. A cocrystal strategy to tune the luminescent properties of stilbene-type organic solid-state materials. *Angew. Chem., Int. Ed.* **2011**, *50*, 12483−12486.
(18) Wang, Y.; Zhu, W. G.; Du, W. N.; Liu, X. F.; Zhang, X. T.; Dong, H. L.; Hu, W. P. Cocrystals strategy towards materials for near-infrared photothermal conversion and imaging. *Angew. Chem., Int. Ed.* **2018**, *57*, 3963−3967.
(19) Erdle, E.; Mohwald, H. Statistical model and experiments on low-dimensional exciton transport. *Phys. Stat. Sol. (b)* **1980**, *98*, 617−621.
(20) Agostini, G.; Corvaja, C.; Giacometti, G.; Pasimeni, L.; Clemente, D. A.; Bandoli, G. Crystal structure of the 1:1 CT complex of biphenylene with 1,2,4,5-tetracyanobenzene and EPR of photo-excited triplet excitions. *Mol. Cryst. Liq. Cryst.* **1986**, *141*, 165−178.
(21) Dalal, N. S.; Haarer, D.; Bargon, J.; Mohwald, H. ESR study of the hyperfine structure of the triplet state in crystalline donor acceptor complexes: A probe for the degree of charge transfer in the excited state. *Chem. Phys. Lett.* **1976**, *40*, 326−330.
(22) Haarer, D.; Karl, N. Charge transfer absorption, CT-emission, and ESR spectroscopy with zone refined crystals of anthracene-pyromellitic dianhydride. *Chem. Phys. Lett.* **1973**, *21*, 49−53.
(23) Keijzers, C. P.; Haarer, D. The symmetry of a triplet charge transfer state in phenanthrene-PMDA crystals: Dimer versus trimer. *Chem. Phys. Lett.* **1977**, *49*, 24−28.
(24) Keijzers, C. P.; Haarer, D. EPR spectroscopy of delocalized and localized charge-transfer excitons in phenanthrene-PMDA single crystals. *J. Chem. Phys.* **1977**, *67*, 925−932.
(25) Maniero, A. L.; Toffoletti, A.; Corvaja, C. ENDOR spectra of 2-methyl-naphthalene-TCNB triplet trap in naphthalene-TCNB single crystals. *Z. Naturforsch.* **1993**, *48*, 497−504.
(26) Nothe, D.; Moroni, W.; Keller, H.J.; Soos, Z.G.; Mazumdar, S. Triplet spin excitons in organic charge-transfer complexes. *Solid State Commun.* **1978**, *26*, 713−716.
(27) Pasimeni, L.; Corvaja, C. EPR studies of electron spin polarization of triplet exciton and its transfer into triplet traps of naphthalene-TCNQ and naphthalene-p-chloranil guest complexes in the naphthalene-TCNB host. *Mol. Cryst. Liq. Cryst.* **1983**, *100*, 17−29.
(28) Pasimeni, L.; Guella, G.; Corvaja, C.; Clemente, D. A.; Vicentini, M. Crystal structure of biphenyl-1,2,4,5-tetracyanobenzene 1:1 CT complex and EPR investigation of photoexcited triplet excitons. *Mol. Cryst. Liq. Cryst.* **1983**, *91*, 25−38.
(29) Zukun, W.; Wu, R. H.; Chen, Z.; Ye, L.; Li, H. Y.; Zhu, H. M. Ultrafast electron transfer before singlet fission and slow triplet state electron transfer in pentacene single crystal/C-60 heterostructure. *J. Phys. Chem. A* **2020**, *124*, 4185−4192.
(30) He, G. Y.; Busby, E.; Appavoo, K.; Wu, Q.; Xia, J. L.; Campos, L. M.; Sfeir, M. Y. Charge transfer states impact the triplet pair dynamics of singlet fission polymers. *J. Chem. Phys.* **2020**, *153*, 244902.
(31) Ogawa, T.; Hosoyamada, M.; Yurash, B.; Nguyen, T. Q.; Yanai, N.; Kimizuka, N. Donor-acceptor-collector ternary crystalline films for efficient solid-state photon upconversion. *J. Am. Chem. Soc.* **2018**, *140*, 8788−8796.
(32) Hosoyamada, M.; Yanai, N.; Ogawa, T.; Kimizuka, N. Molecularly dispersed donors in acceptor molecular crystals for photon upconversion under low excitation intensity. *Chem. Eur. J.* **2016**, *22*, 2060−2067.
(33) Wang, Z. J.; Ivanov, M.; Gao, Y. T.; Bussotti, L.; Foggi, P.; Zhang, H. M.; Russo, N.; Dick, B.; Zhao, J. Z.; Di Donato, M.; Mazzone, G.; Luo, L.; Fedin, M. Spin-orbit charge-transfer intersystem crossing (ISC) in compact electron donor-acceptor dyads: ISC mechanism and application as novel and potent photodynamic therapy reagents. *Chem. Eur. J.* **2020**, *26*, 1091−1102.
(34) Zhao, Y. J.; Sukhanov, A. A.; Duan, R. M.; Elmali, A.; Hou, Y. Q.; Zhao, J. Z.; Gurzadyan, G. G.; Karatay, A.; Voronkova, V. K.; Li, C. Study of the spin-orbit charge transfer intersystem crossing of perylenemonoimide-phenothiazine compact electron donor/acceptor dyads with steady-state and time-resolved optical and magnetic spectroscopies. *J. Phys. Chem. C* **2019**, *123*, 18270−18282.

https://doi.org/10.1021/jacs.2c08584
J. Am. Chem. Soc. 2022, 144, 18607−18618

(35) Zhao, Y.; Duan, R.; Zhao, J.; Li, C. Spin-orbit charge transfer intersystem crossing in perylenemonoimide-phenothiazine compact electron donor-acceptor dyads. *Chem. Commun.* **2018**, *54*, 12329−12332.
(36) Williams, R. M.; Zwier, J. M.; Verhoeven, J. W. Photoinduced intramolecular electron-transfer in a bridged C-60 (acceptor) aniline (donor) system - photophysical properties of the first active fullerene diad. *J. Am. Chem. Soc.* **1995**, *117*, 4093−4099.
(37) Colvin, M. T.; Ricks, A. B.; Scott, A. M.; Co, D. T.; Wasielewski, M. R. Intersystem crossing involving strongly spin exchange-coupled radical ion pairs in donor-bridge-acceptor molecules. *J. Phys. Chem. A* **2012**, *116*, 1923−1930.
(38) Hou, Y. Q.; Kurganskii, I.; Elmali, A.; Zhang, H. M.; Gao, Y. T.; Lv, L. L.; Zhao, J. Z.; Karatay, A.; Luo, L.; Fedin, M. Electronic coupling and spin-orbit charge transfer intersystem crossing (SOCT-ISC) in compact BDP-carbazole dyads with different mutual orientations of the electron donor and acceptor. *J. Chem. Phys.* **2020**, *152*, 114701.
(39) Smith, M. B.; Michl, J. Singlet fission. *Chem. Rev.* **2010**, *110*, 6891−6936.
(40) Young, R. M.; Wasielewski, M. R. Mixed electronic states in molecular dimers: Connecting singlet fission, excimer formation, and symmetry-breaking charge transfer. *Acc. Chem. Res.* **2020**, *53*, 1957−1968.
(41) Harvey, S. M.; Wasielewski, M. R. Photogenerated spin-correlated radical pairs: From photosynthetic energy transduction to quantum information science. *J. Am. Chem. Soc.* **2021**, *143*, 15508−15529.
(42) Dance, Z. E. X.; Mi, Q.; McCamant, D. W.; Ahrens, M. J.; Ratner, M. A.; Wasielewski, M. R. Time-resolved EPR studies of photogenerated radical ion pairs separated by p-phenylene oligomers and of triplet states resulting from charge recombination. *J. Phys. Chem. B* **2006**, *110*, 25163−25173.
(43) Dance, Z. E. X.; Mickley, S. M.; Wilson, T. M.; Ricks, A. B.; Scott, A. M.; Ratner, M. A.; Wasielewski, M. R. Intersystem crossing mediated by photoinduced intramolecular charge transfer: Julolidine-anthracene molecules with perpendicular π systems. *J. Phys. Chem. A* **2008**, *112*, 4194−4201.
(44) Ni, W. J.; Gurzadyan, G. G.; Ma, L.; Hu, P.; Kloc, C.; Sun, L. C. Ultrafast tuning of various photochemical pathways in perylene-tcnq charge-transfer crystals. *J. Phys. Chem. C* **2020**, *124*, 13894−13901.
(45) Buck, J. T.; Boudreau, A. M.; DeCarmine, A.; Wilson, R. W.; Hampsey, J.; Mani, T. Spin-allowed transitions control the formation of triplet excited states in orthogonal donor-acceptor dyads. *Chem.* **2019**, *5*, 138−155.
(46) Schlesinger, I.; Powers-Riggs, N. E.; Logsdon, J. L.; Qi, Y.; Miller, S. A.; Tempelaar, R.; Young, R. M.; Wasielewski, M. R. Charge-transfer biexciton annihilation in a donor-acceptor co-crystal yields high-energy long-lived charge carriers. *Chem. Sci.* **2020**, *11*, 9532−9541.
(47) Rehmat, N.; Toffoletti, A.; Mahmood, Z.; Zhang, X.; Zhao, J. Z.; Barbon, A. Carbazole-perylenebisimide electron donor/acceptor dyads showing efficient spin orbit charge transfer intersystem crossing (SOCT-ISC) and photo-driven intermolecular electron transfer. *J. Mater. Chem. C* **2020**, *8*, 4701−4712.
(48) Dong, Y.; Sukhanov, A. A.; Zhao, J.; Elmali, A.; Li, X.; Dick, B.; Karatay, A.; Voronkova, V. K. Spin-orbit charge-transfer intersystem crossing (SOCT-ISC) in bodipy-phenoxazine dyads: Effect of chromophore orientation and conformation restriction on the photophysical properties. *J. Phys. Chem. C* **2019**, *123*, 22793−22811.
(49) Zhu, T.; Wan, Y.; Huang, L. Direct imaging of Frenkel exciton transport by ultrafast microscopy. *Acc. Chem. Res.* **2017**, *50*, 1725−1733.
(50) Demmig, S.; Langhals, H. Very soluble and photostable perylene fluorescent dyes. *Chem. Ber.* **1988**, *121*, 225−30.
(51) Myong, M. S.; Qi, Y.; Stern, C.; Wasielewski, M. R. Ultrafast photo-driven charge transfer exciton dynamics in mixed-stack pyrene-perylenediimide single co-crystals. *J. Mater. Chem. C* **2021**, *9*, 16911−16917.
(52) Sheldrick, G. M. Crystal structure refinement with shelxt. *Acta Crystallogr. A Struct. Chem.* **2015**, *71*, 3−8.
(53) Dolomanov, O. V.; Bourhis, L. J.; Gildea, R. J.; Howard, J. A. K.; Puschmann, H. Olex2: A complete structure solution, refinement and analysis program. *J. Appl. Crystallogr.* **2009**, *42*, 339−341.
(54) Margulies, E. A.; Logsdon, J. L.; Miller, C. E.; Ma, L.; Simonoff, E.; Young, R. M.; Schatz, G. C.; Wasielewski, M. R. Direct observation of a charge-transfer state preceding high-yield singlet fission in terrylenediimide thin films. *J. Am. Chem. Soc.* **2017**, *139*, 663−671.
(55) Stoll, S.; Schweiger, A. Easyspin, a comprehensive software package for spectral simulation and analysis in EPR. *J. Magn. Reson.* **2006**, *178*, 42−55.
(56) Shao, Y.; Gan, Z.; Epifanovsky, E.; Gilbert, A. T. B.; Wormit, M.; Kussmann, J.; Lange, A. W.; Behn, A.; Deng, J.; Feng, X.; Ghosh, D.; Goldey, M.; Horn, P. R.; Jacobson, L. D.; Kaliman, I.; Khaliullin, R. Z.; Kuś, T.; Landau, A.; Liu, J.; Proynov, E. I.; Rhee, Y. M.; Richard, R. M.; Rohrdanz, M. A.; Steele, R. P.; Sundstrom, E. J.; Woodcock, H. L.; Zimmerman, P. M.; Zuev, D.; Albrecht, B.; Alguire, E.; Austin, B.; Beran, G. J. O.; Bernard, Y. A.; Berquist, E.; Brandhorst, K.; Bravaya, K. B.; Brown, S. T.; Casanova, D.; Chang, C.-M.; Chen, Y.; Chien, S. H.; Closser, K. D.; Crittenden, D. L.; Diedenhofen, M.; DiStasio, R. A.; Do, H.; Dutoi, A. D.; Edgar, R. G.; Fatehi, S.; Fusti-Molnar, L.; Ghysels, A.; Golubeva-Zadorozhnaya, A.; Gomes, J.; Hanson-Heine, M. W. D.; Harbach, P. H. P.; Hauser, A. W.; Hohenstein, E. G.; Holden, Z. C.; Jagau, T.-C.; Ji, H.; Kaduk, B.; Khistyaev, K.; Kim, J.; Kim, J.; King, R. A.; Klunzinger, P.; Kosenkov, D.; Kowalczyk, T.; Krauter, C. M.; Lao, K. U.; Laurent, A. D.; Lawler, K. V.; Levchenko, S. V.; Lin, C. Y.; Liu, F.; Livshits, E.; Lochan, R. C.; Luenser, A.; Manohar, P.; Manzer, S. F.; Mao, S.-P.; Mardirossian, N.; Marenich, A. V.; Maurer, S. A.; Mayhall, N. J.; Neuscamman, E.; Oana, C. M.; Olivares-Amaya, R.; O'Neill, D. P.; Parkhill, J. A.; Perrine, T. M.; Peverati, R.; Prociuk, A.; Rehn, D. R.; Rosta, E.; Russ, N. J.; Sharada, S. M.; Sharma, S.; Small, D. W.; Sodt, A.; Stein, T.; Stück, D.; Su, Y.-C.; Thom, A. J. W.; Tsuchimochi, T.; Vanovschi, V.; Vogt, L.; Vydrov, O.; Wang, T.; Watson, M. A.; Wenzel, J.; White, A.; Williams, C. F.; Yang, J.; Yeganeh, S.; Yost, S. R.; You, Z.-Q.; Zhang, I. Y.; Zhang, X.; Zhao, Y.; Brooks, B. R.; Chan, G. K. L.; Chipman, D. M.; Cramer, C. J.; Goddard, W. A.; Gordon, M. S.; Hehre, W. J.; Klamt, A.; Schaefer, H. F.; Schmidt, M. W.; Sherrill, C. D.; Truhlar, D. G.; Warshel, A.; Xu, X.; Aspuru-Guzik, A.; Baer, R.; Bell, A. T.; Besley, N. A.; Chai, J.-D.; Dreuw, A.; Dunietz, B. D.; Furlani, T. R.; Gwaltney, S. R.; Hsu, C.-P.; Jung, Y.; Kong, J.; Lambrecht, D. S.; Liang, W.; Ochsenfeld, C.; Rassolov, V. A.; Slipchenko, L. V.; Subotnik, J. E.; Van Voorhis, T.; Herbert, J. M.; Krylov, A. I.; Gill, P. M. W.; Head-Gordon, M. Advances in molecular quantum chemistry contained in the Q-chem 4 program package. *Mol. Phys.* **2015**, *113*, 184−215.
(57) Lu, T.; Chen, F. Multiwfn: A multifunctional wavefunction analyzer. *J. Comput. Chem.* **2012**, *33*, 580−592.
(58) Wang, C.; Wang, J.; Wu, N.; Xu, M.; Yang, X.; Lu, Y.; Zang, L. Donor-acceptor single cocrystal of coronene and perylene diimide: Molecular self-assembly and charge-transfer photoluminescence. *RSC Adv.* **2017**, *7*, 2382−2387.
(59) Ohno, K.; Inokuchi, H. Polarized absorption, fluorescence and phosphorescence spectra of coronene in triphenylene matrix at 4.2°K. *Chem. Phys. Lett.* **1973**, *23*, 561−566.
(60) Würthner, F.; Saha-Moller, C. R.; Fimmel, B.; Ogi, S.; Leowanawat, P.; Schmidt, D. Perylene bisimide dye assemblies as archetype functional supramolecular materials. *Chem. Rev.* **2016**, *116*, 962−1052.
(61) Würthner, F.; Saha-Möller, C. R.; Fimmel, B.; Ogi, S.; Leowanawat, P.; Schmidt, D. Perylene bisimide dye assemblies as archetype functional supramolecular materials. *Chem. Rev.* **2016**, *116*, 962−1052.
(62) Taratula, O.; Rochford, J.; Piotrowiak, P.; Galoppini, E.; Carlisle, R. A.; Meyer, G. J. Pyrene-terminated phenylenethynylene rigid linkers anchored to metal oxide nanoparticles. *J. Phys. Chem. B* **2006**, *110*, 15734−15741.
(63) Gosztola, D.; Niemczyk, M. P.; Svec, W.; Lukas, A. S.; Wasielewski, M. R. Excited doublet states of electrochemically

https://doi.org/10.1021/jacs.2c08584
J. Am. Chem. Soc. 2022, 144, 18607−18618

generated aromatic imide and diimide radical anions. *J. Phys. Chem. A* **2000**, *104*, 6545−6551.
(64) Pysh, E. S.; Yang, N. C. Polarographic oxidation potentials of aromatic compounds. *J. Am. Chem. Soc.* **1963**, *85*, 2124−2130.
(65) Weller, A. Photoinduced electron transfer in solution: Exciplex and radical ion pair formation free enthalpies and their solvent dependence. *Z. Phys. Chem.* **1982**, *133*, 93−99.
(66) Kong, J.; Zhang, W.; Li, G.; Huo, D.; Guo, Y.; Niu, X.; Wan, Y.; Tang, B.; Xia, A. Excited-state symmetry-breaking charge separation dynamics in multibranched perylene diimide molecules. *J. Phys. Chem. Lett.* **2020**, *11*, 10329−10339.
(67) Khan, Z. H. Electronic-spectra of radical cations and their correlation with photoelectron-spectra—III. Perylenes and coronenes. *Spectrochim. Acta Part A* **1988**, *44*, 313−320.
(68) Yu, Z.; Wu, Y.; Peng, Q.; Sun, C.; Chen, J.; Yao, J.; Fu, H. Accessing the triplet state in heavy-atom-free perylene diimides. *Chem. Eur. J.* **2016**, *22*, 4717−4722.
(69) Shida, T.; Iwata, S. Electronic spectra of ion radicals and their molecular orbital interpretation. III. Aromatic hydrocarbons. *J. Am. Chem. Soc.* **1973**, *95*, 3473−3483.
(70) Bullock, J. E.; Carmieli, R.; Mickley, S. M.; Vura-Weis, J.; Wasielewski, M. R. Photoinitiated charge transport through π-stacked electron conduits in supramolecular ordered assemblies of donor-acceptor triads. *J. Am. Chem. Soc.* **2009**, *131*, 11919−11929.
(71) Levanon, H.; Norris, J. R. The photoexcited triplet-state and photosynthesis. *Chem. Rev.* **1978**, *78*, 185−198.
(72) de Groot, M. S.; van der Waals, J. H. Paramagnetic resonance in phosphorescent aromatic hydrocarbons. *Mol. Phys.* **1960**, *3*, 190−200.
(73) Hasharoni, K.; Levanon, H.; Greenfield, S. R.; Gosztola, D. J.; Svec, W. A.; Wasielewski, M. R. Radical pair and triplet state dynamics of a photosynthetic reaction-center model embedded in isotropic media and liquid crystals. *J. Am. Chem. Soc.* **1996**, *118*, 10228−10235.
(74) Maruani, J.; Kite, T. M.; Korb, J. P.; Gille, X. Spin relaxation of triplet pyrene in a crystal and in a glass. *Mol. Phys.* **1978**, *36*, 1261−1299.
(75) Weiss, L. R.; Bayliss, S. L.; Kraffert, F.; Thorley, K. J.; Anthony, J. E.; Bittl, R.; Friend, R. H.; Rao, A.; Greenham, N. C.; Behrends, J. Strongly exchange-coupled triplet pairs in an organic semiconductor. *Nat. Phys.* **2017**, *13*, 176−181.
(76) Turro, N. J.; Ramamurthy, V.; Scaiano, J. C. *Modern Molecular Photochemistry of Organic Molecules*; University Science Books: Sausalito, CA, 2010; p 1084.
(77) Liu, D.; El-Zohry, A. M.; Taddei, M.; Matt, C.; Bussotti, L.; Wang, Z.; Zhao, J.; Mohammed, O. F.; Di Donato, M.; Weber, S. Long-lived charge-transfer state induced by spin-orbit charge transfer intersystem crossing (SOCT-ISC) in a compact spiro electron donor/acceptor dyad. *Angew. Chem., Int. Ed.* **2020**, *59*, 11591−11599.
(78) Closs, G. L.; Miller, J. R. Intramolecular long-distance electron transfer in organic molecules. *Science* **1988**, *240*, 440−447.
(79) Weiss, E. A.; Sinks, L. E.; Lukas, A. S.; Chernick, E. T.; Ratner, M. A.; Wasielewski, M. R. Influence of energetics and electronic coupling on through-bond and through-space electron transfer within u-shaped donor-bridge-acceptor arrays. *J. Phys. Chem. B* **2004**, *108*, 10309−10316.
(80) Weiss, E. A.; Tauber, M. J.; Kelley, R. F.; Ahrens, M. J.; Ratner, M. A.; Wasielewski, M. R. Conformationally gated switching between superexchange and hopping within oligo-*p*-phenylene-based molecular wires. *J. Am. Chem. Soc.* **2005**, *127*, 11842−11850.
(81) Marcus, R. A. On the theory of oxidation-reduction reactions involving electron transfer. I. *J. Chem. Phys.* **1956**, *24*, 966−978.
(82) Marcus, R. A. On the theory of electron-transfer reactions. VI. Unified treatment for homogeneous and electrode reactions. *J. Chem. Phys.* **1965**, *43*, 679−701.

https://doi.org/10.1021/jacs.2c08584
J. Am. Chem. Soc. 2022, 144, 18607−18618